PNAS
www.pnas.org

Supplementary Information for

No evidence of canopy-scale leaf thermoregulation to cool leaves below air temperature across a range of forest ecosystems

Authors: Still*, C.J., Page, G.F.M., Griffith, D.M., Rastogi., B., Aubrecht, D.M., Kim, Y., Burns, S.P., Hanson, C.V., Kwon, H., Hawkins, L., Meinzer, F.C., Sevanto, S., Roberts, D.A., Goulden, M., Pau, S., Detto, M., Helliker, B.R., and Richardson, A.D.

Christopher Still
Email: chris.still@oregonstate.edu

This PDF file includes:

- Supplementary text
- Figures S1 to S9
- Tables S1 to S1
- SI References

Supplementary Information Text

Site thermal data acquisition and analysis

T_{leaf} observations were collected using thermal cameras from multiple forest research sites in North and Central America (Tables S1, S2) to assess how and when leaf homeothermy can occur. Using thermal cameras assumes a certain object emissivity and corrections for reflected downwelling thermal infrared radiation. Important variables were included in the correction procedure outlined by (1, 2) to account for environmental influences on temperatures measured by our cameras. We assumed a canopy-scale leaf emissivity of 0.98. In almost all cases the corrections were small (< 1K), with the largest changes for morning periods following cold nights (at Metolius, Wind River, Pinyon Flat, and Niwot Ridge). At each site, regions of interest (ROIs) containing leaves were selected from imagery and the values across ROIs were averaged to calculate T_{leaf} at the level of the entire canopy (T_{can}), at the species level (HF), or at the level of leaf habit (BCI), and only when trees were leafed out. Cameras were pointed north (facing sunlit canopies) at all sites except for the tropical one (BCI) with high solar angles. This camera faced southwest toward the canopy around the eddy flux system. Other site imaging details are discussed elsewhere (1, 3–6).

Metolius

A thermal camera (FLIR A325sc, FLIR System Inc., Wilsonville, OR, USA) on a fixed-mount was used to capture TIR images. The camera was housed inside a FLIR standard enclosure to protect the camera from rain and frost. The camera and housing were upright and positioned to face north-northwest to avoid direct sunlight. The pixel resolution of this camera model is 360 × 240 pixels; a FLIR IR 30-mm lens (focal length: 30.38 mm; field of view: 15º × 11.25º) was used for image collection. Within the field of view (FOV), spot sizes of a single pixel are 0.83 cm from 10-m distance and 8.3 cm from 100-m distance. This camera uses an uncooled microbolometer detector to scan the longwave spectra ranging from 7.5 to 13.0 µm. The maximum frame rate for recording is 60 Hz, and the external air temperature operating range is –20 to 120 ºC. A fanless computer (PC) was used to control the camera and collect images using the Gigabit Ethernet data streaming protocol for connection between the camera and PC. FLIR ResearchIR 3.4 SP2 software was used to control the camera and collect images. The measurement interval was fixed at 5 minutes throughout the 2015 growing season, creating 288 images per day during when the system was continuously operational. ROIs were selected as described in (3). Sub-hourly data were further averaged to the hour. Data was filtered from day of year 115 to 260 in 2015.

Wind River

The same type of thermal camera system deployed at Metolius was used to capture TIR images from Wind River. However, the camera was mounted on a pan-tilt system (FLIR PTU-D100E, FLIR System Inc., Wilsonville, OR) to image a large area of the forest, and in particular to measure multiple canopy heights to capture vertical changes in canopy thermal states. PTU movements were controlled via a terminal emulator program running in a PC located inside an instrument shed at the base of the flux tower. Approximately 60-m length ethernet and telephone cables were used to connect between the PC in the shed and the thermal camera and PTU on the tower. We selected ten PTU angle positions for the canopy measurement across the vertical profile from the bottom to top canopy layers. Five PTU positions were focused on the upper canopy, ~40 to 60 m in height, and the remaining five PTU positions imaged the mid-level canopy (~20 to 50 m at height) and lower-level canopy layers (~0 to 30 m at height). The measurement interval for each PTU position was 6 minutes (one complete cycle over 60 minutes) during the 2015 growing season. For this study, ROIs from the upper, sunlit canopy PTU positions were averaged together. Sub-hourly data were averaged to the hour. Data was filtered from day of year 70 to 258 in 2015.

Niwot Ridge

An instrument package similar to the one at Harvard Forest was deployed in 2015 at the 26 m tall Ameriflux tower at the Mountain Research Station operated by the University of Colorado. This package includes an A655sc camera (FLIR Systems, Inc., 640 × 480 pixel resolution, 45º FOV), mounted near the top of the tower and pointed east with an inclination ~ 30º below the horizon. Supporting measurements were made using instrumentation similar to the Harvard Forest site. Image acquisition was performed by FLIR's ResearchIR software running on a fanless industrial computer mounted on the tower. For more details see (1). Data was filtered from day of year 100 to 310 (collection spanning years 2015 to 2019).

Pinyon Flat

A thermal camera (FLIR A325sc, FLIR System Inc.) mounted on a pan-tilt system (FLIR PTU-D100E, FLIR System Inc.) was installed on the flux tower to capture TIR images. Further information about image collection and processing can be found at: https://faculty.sites.uci.edu/mgoulden/development-of-tower-based-tools-for-quantifying-vegetation-distribution-and-health/. Data was filtered from day of year 135 to 288 (collection spanning years 2013 to 2015).

Harvard Forest

The thermal camera (model A655sc from FLIR Systems, Inc., 640 × 480 pixel resolution, 45ºFOV) was mounted on the 40 m tall "Barn Tower" (42.5353◦ N 72.1899◦ W, elev. 350 m ASL), The camera was installed in 2013. Images were acquired continuously every 15 min by FLIR's ExaminIR software running on fanless industrial computers (Neousys POC-100, Logic Supply, Inc.) at the base of the tower and connected to the camera via Ethernet. Within the thermal images, we extracted temperature information for upper-canopy (i.e., potentially exposed to full sunlight for some or all of the day) foliage from the dominant tree species. Full details of the setup and image processing are given by (1). Data was filtered from day of year 135 to 288 in 2015.

Barro Colorado Island

At this site a FLIR A325sc thermal camera (FLIR System Inc.) was installed on a telecommunications tower 40 m above ground (10 m above mean canopy height) and connected with a 50 m Ethernet cable to a laptop located in a shed under the tower. The camera was facing southwest to capture high-frequency TIR images in the footprint of an eddy covariance tower located about 150 m from the telecommunication tower. Images were collected every 5 minutes from February 17 to September 30, 2015, for a total of 288 images per day. Continuous measurements were interrupted between August 3-6, 2015. In total, 5198 images were captured across 257 days. Within the FOV, a single pixel spot size is 0.14 cm from 1 m, 1.4 cm from 10 m, 6.9 cm from 50 m, and 20.8 cm from 150 m in a single pixel. Each ROI was 2 by 2 pixels and effective pixel sizes ranged between ~7 and 20 cm depending on distance. Full details of the setup and image processing are given by (5). Data period filtered from day of year 48 to 252 in 2015.

Tower flux, meteorological, and radiation data

Metolius (AMERIFLUX site US-Me-2)

Eddy-covariance (EC) measurements at MR were conducted using a 3-D sonic anemometer (model CSAT3, Campbell Scientific Inc., Logan, UT, USA) and a closed-path infrared gas analyzer (model LI-7200, LI-COR Inc., Lincoln, NE, USA) at a height of 33.0 m. CO_2 storage is measured using a profile system (7 heights, model LI-820, LI-COR Inc.) Processing of high frequency data follow Kwon et al. (2018) and Thomas et al. (2009). GPP was calculated as the residual of NEE and Re. Partitioned data were gap filled using the online tool REddyProc. Thirty-minute fluxes are calculated using outlier removal of turbulent variables in raw data and rigorous quality control of initial 30-min flux data using a combination of higher-order statistics and quality flags for stationarity. After removing unsatisfactory flagged data, gap-filling was conducted separately for CO_2 and H_2O fluxes. Meteorological measurements include a 4-component radiometer (model CNR1, Kipp & Zonen, Delft, The Netherlands) and air temperature and relative humidity (model HMP45, Vaisala, Helsinki, Finland) at 31.6 m. More details on flux data processing and instrument can be found in (7, 8). All flux data were from the 2015 growing season and corresponded to the same DOY filters as the thermal data.

Wind River (AMERIFLUX site US-Wrc)

Carbon, water, and energy fluxes have been collected since 1998 using the EC technique at the Wind River tower. The most recent EC system consists of a 3-D sonic anemometer (CSAT3, Campbell Scientific Inc.) and a closed-path infrared gas analyzer (LI-7000, Li-COR Inc.). The EC system is located approximately 10 m above the canopy top at a height of 70 m. NEE was partitioned into ecosystem respiration (Re) and GPP by identifying a turbulence (friction velocity) threshold, fitting an exponential temperature response curve to the nighttime NEE, and extrapolating the relationship to calculate daytime Re. GPP was calculated as the residual of NEE and Re. Partitioned data were gap filled using the online tool REddyProc. Measurements of radiation and temperature and relative humidity were conducted using a 4-component radiometer (CNR1, Kipp & Zonen) and a temperature/humidity sensor (HMP45-C, Vaisala) at 70.0 m. For flux data processing and instrument details see (9). All flux data were from the 2015 growing season and corresponded to the same DOY filters as the thermal data.

Niwot Ridge (AMERIFLUX site US-NR1)

Fluxes of CO_2, H_2O, and sensible heat were measured at 21.5 m on the main tower using a 3-D sonic anemometer (CSAT3, Campbell Scientific Inc.), krypton hygrometer (model KH2O, Campbell Scientific Inc.), and closed-path infrared gas analyzers (model LI-6262 and LI-7200, LI-COR Inc.). Flux data were processed using standard EC flux data-processing techniques. Prior to the flux calculations, the measured wind components were transformed into streamline coordinates using the planar-fit method. For sensible heat flux, corrections to the sonic temperature following (10) were applied. To calculate CO_2 storage, a vertical profile of CO_2 was measured at the tower between years 1999-2016 (11) and has been modeled since 2016. GPP was calculated as the residual of NEE and Re. Partitioned data were gap filled using the online tool REddyProc. Radiation was measured with a 4-component radiometer (CNR1, Kipp & Zonen) mounted at 25.5 m. Temperature and relative humidity profiles were measured with three mechanically aspirated, slow-response temperature-humidity sensors (model HMP35-D, Vaisala) installed at 2, 8, and 21.5 m AGL. Further details about the US-NR1 site instrumentation and data processing can be found elsewhere (11, 12). All flux data were from the 2016 growing season and corresponded to the same DOY filters as the thermal data.

Pinyon Flat (AMERIFLUX site US-SCw)

Further information about data processing can be found at: https://ameriflux.lbl.gov/sites/siteinfo/US-SCw.

Harvard Forest (AMERIFLUX site US-Ha-1)

EC flux data were collected at the environmental measurement site tower located 2 km to the east of the thermal camera in a forest stand of similar composition. For data processing and instrumentation details, see (13). GPP was calculated as the residual of NEE and Re. Partitioned data were gap filled using the online tool REddyProc. All flux data were from the 2015 growing season and corresponded to the same DOY filters as the thermal data.

Barro Colorado Island (AMERIFLUX site PA-Bar)

The tower used for these measurements is 41 m above ground, on a plateau on BCI. The EC system includes a 3-D sonic anemometer (CSAT3, Campbell Scientific Inc,) and an open-path infrared gas analyzer (LI7500, LI-COR Inc.). High-frequency (10Hz) EC data were processed with a custom program using a standard routine described in (14). GPP was derived from daytime values of NEE by adding the corresponding mean daily Re obtained as the intercept of the light-response curve (15). The light curve was fitted on a 15-day moving window using a rectangular hyperbolic function using data after excluding friction velocities < 0.4 m s^{-1}. Shortwave and longwave radiations were measured using a 4-component radiometer (CNR1, Kipp & Zonen). Air temperature and relative humidity were measured by a HC2S3 probe (Campbell Scientific Inc.) enclosed in a radiation shield. All flux data were from the 2015 growing season and corresponded to the same DOY filters as the thermal data.

Calculation of T_{aero} and T_{LW}

T_{aero} and T_{LW} were calculated using the R package, bigleaf (16). T_{LW} was estimated using a surface emissivity of 0.98. T_{aero} was calculated from measured sensible heat fluxes and the aerodynamic conductance for heat transfer based on canopy structural values from Tables S1 and S2. We used the Businger stability correction and the Su et al. formulation for boundary layer resistance in this calculation. However, we recognize the challenges of estimating T_{aero} from sensible heat fluxes over forests with variable roughness lengths for heat (17).

Leaf Energy Balance Modeling

Leaf energy balance theory has long provided a theoretical and conceptual framework for understanding the factors that regulate T_{leaf} and its interactions with ambient microclimate and radiative forcing (18). A leaf reflects, absorbs, and transmits shortwave (SW) radiation, and also absorbs and emits longwave (LW) radiation. Thus, the net radiation budget for a single leaf is a function of absorbed solar shortwave radiation (SW, in W m^{-2}) and the net of absorbed and emitted longwave radiation (LW, in W m^{-2}) (19–21). For temperature modeling, it is preferable to use the isothermal net radiation (R_{niso}, in W m^{-2}), which is independent of T_{leaf} and describes the net radiation of a surface at air temperature (21), and thus can be larger or smaller than R_{net}. For our canopy-scale leaf modeling we used site-level measured radiation fluxes to calculate R_{niso} as follows (where SW_{net} is the net of downwelling and upwelling SW radiation):

$$R_{niso} = \alpha SW_{net} + \alpha_{IR} LW_{down} - \alpha_{IR} \sigma T_{air}{}^4 \qquad 1$$

In this equation, α represents leaf absorptance of *SW* radiation (assumed value of 0.5), α_{IR} is the longwave absorptance/emissivity of a leaf (assumed value of 0.98), σ is the Stefan-Boltzmann constant (5.67×10^{-8} W m^{-2} K^{-4}), and T_{air} is in K. Assuming energy balance closure and negligible heat storage and metabolic energy production, the temperature of a single leaf at steady state can be predicted by this equation (19, 22, 23):

$$T_{leaf} = T_{air} + \Delta T = T_{air} + Y\frac{R_{niso} - LE}{C_p M_{air} g_{bH}} \qquad 2$$

LE is the leaf latent heat flux (W m^{-2}), M_{air} is the molecular mass of air (0.029 kg mol^{-1}), C_p is the specific heat capacity of air (1010 J kg^{-1} ºC^{-1}), and g_{bH} is the 2-sided leaf boundary layer conductance to heat (mol m^{-2} s^{-1}). The *Y* term captures the ratio of g_{bH} to the sum of g_{bH} and the conductance to radiative heat transfer, g_R (mol m^{-2} s^{-1}), following (23). In short, T_{leaf} departs from T_{air} as a function of leaf radiation balance and sensible and latent heat energy exchanges. This equation shows that sufficiently large *LE* can exceed R_{niso} and thus reduce T_{leaf} below T_{air} (24). Because available R_{net} is partitioned into *LE* and leaf sensible heat flux (*H*), such a condition also implies that *H* would be negative, an underappreciated outcome of leaf homeothermy that we evaluate using site-level EC heat flux data.

There are multiple ways to calculate leaf transpiration (*LE*). Most approaches default to either a flux determined by stomatal conductance and the vapor pressure driving gradient (*VPD*), or a flux determined by the net absorbed radiation available for driving evaporation (22, 25). In understanding the conditions that force leaves to be cooler or warmer than surrounding air as a function of different transpiration models, the concept of leaf-to-air coupling is useful. This is captured by the decoupling coefficient (Ω), which is defined mathematically as (22, 26):

$$\Omega = \frac{\varepsilon + 2 + \frac{g_R}{g_{bH}}}{\varepsilon + \frac{g_R + g_{bH}}{g_s} + \frac{g_R}{g_{bH}}} \qquad 3$$

where ε is the ratio of s/γ (the ratio of the slope of saturated vapor pressure versus temperature curve to the psychrometric constant, both of which are temperature dependent with units of Pa K^{-1}). The leaf stomatal conductance to water vapor is g_s (described below), while g_{bH} (mol m^{-2} s^{-1}) is calculated separately for needleleaf (NL) and broadleaf (BL) plants following (27); see also (19)) for turbulent conditions and ignoring free convection as:

$$g_{bH-NL} = 0.006\rho_{mol}\frac{u^{0.6}}{d^{0.4}} \qquad 4a$$

$$g_{bH-BL} = 0.0105\rho_{mol}\frac{u^{0.5}}{d^{0.5}} \qquad 4b$$

where *d* is the leaf characteristic dimension (m) taken as leaf width, *u* is the measured horizontal windspeed (m s^{-1}), and ρ_{mol} (mol m^{-3}) is the molar density of air to convert conductance from m s^{-1} to mol m^{-2} s^{-1}. The resulting value of g_{bH} for each leaf type is multiplied by 2 to capture both sides of a leaf (20, 28). For the semi-arid pine site (Metolius, USA), a characteristic leaf dimension of 0.01 m was assumed for a bundle of needles, while for the tropical forest site (BCI, Panama) a value of 0.1 m was used. *P* is atmospheric pressure (Pa), T_{airK} is air temperature in Kelvin, and *R* is the ideal gas constant (8.3144 J mol^{-1} K^{-1}). g_R, multiplied by 2 for both leaf sides, is calculated as:

$$g_R = 2\rho_{mol}\frac{4\alpha_{IR}\sigma {T_{airK}}^3}{\rho C_p} \qquad 5$$

Ω is a decoupling coefficient, as a value of 1 describes a leaf that is perfectly decoupled to the surrounding air and leads to the radiation-limited, equilibrium transpiration rate (W m^{-2}) as (22, 26):

$$LE_{eq} = \frac{\varepsilon R_{niso}}{\varepsilon + 1 + \frac{g_R}{g_{bH}}} \qquad 6a$$

The equilibrium transpiration rate varies principally with T_{air} and R_{niso}. The term multiplying R_{niso}, ($\varepsilon/(\varepsilon + 1 + g_R/g_{bH})$), represents the fraction of absorbed radiation that is converted to latent heat (25, 29). ε is linearly and positively related to *VPD* and thus implicitly includes a term that affects stomatal conductance as in the fully coupled relationship in equation (6b). The decoupled, equilibrium transpiration is very similar to the Priestley-Taylor formulation, which also includes an empirical modifier for modeling evaporation fluxes across larger spatial scales.

By contrast, an Ω value of 0 describes a leaf that is perfectly coupled to the surrounding air (i.e., very high boundary layer conductances), leading to a stomatally 'imposed' transpiration rate:

$$LE_{imp} = g_{tot}\lambda\frac{(e_{sat} - e_a)}{P} \qquad \text{6b}$$

where g_{tot} is the total water vapor conductance of the leaf (mol m^{-2} s^{-1}) and is calculated as the serial sum of g_s and g_{bV}. g_{bV} is the leaf boundary layer conductance to vapor (each vapor phase conductance is one-sided for hypostomatous leaves as assumed here). g_{bV} is taken to be 1.08 times the value of the one-sided g_{bH} (21, 23). λ is the latent heat of vaporization (44.2 kJ mol^{-1} at 20ºC), e_{sat} - e_a is the vapor pressure deficit of the atmosphere (denoted *D,* Pa), and P_a is atmospheric pressure (Pa).

Leaf latent heat fluxes (*LE*) can then be modeled as the weighted sum of LE_{eq} and LE_{imp} as determined by Ω (21, 22):

$$LE = \Omega LE_{eq} + (1 - \Omega)LE_{imp} \qquad 7$$

Substituting equation (7) into equation (2) yields the following relationship:

$$T_{leaf} = T_{air} + Y\frac{R_{niso} - (\Omega LE_{eq} + (1 - \Omega)LE_{imp})}{C_p M_{air} g_{bH}} \qquad 8$$

In the decoupled, equilibrium extreme (i.e., Ω = 1), equation (8) becomes

$$T_{leaf\_eq} = T_{air} + Y\frac{R_{niso}}{C_p M_{air}}\frac{1 + \frac{g_R}{g_{bH}}}{g_{bH}(\varepsilon + 1) + g_R} \qquad 9$$

In this scenario, as long as R_{niso} is positive, the numerator will be positive and $T_{leaf} > T_{air}$. Importantly, the value of ε increases exponentially with T_{air}, and in the case of constant g_{bH} the warming of T_{leaf} above T_{air} is moderated by increasing ε. For example, at 25ºC, ε = 2.8, and at 35ºC, ε = 4.6. Importantly, the only way for T_{leaf} to be lower than T_{air} in the equilibrium case is to include a Priestley-Taylor modifier following (30), and its importance increases with T_{air}, as that in turn enhances ε, which multiplies the modifier.

In the coupled, imposed extreme (Ω approaches 0), equation (8) becomes:

$$T_{leaf\_imp} = T_{air} + Y\frac{R_{niso} - g_{tot}\lambda\frac{D}{P}}{C_p M_{air} g_{bH}} \qquad 10$$

In this case, a more coupled leaf's transpiration is controlled principally by g_{tot}, and *LE* can exceed R_{niso} and lead to $T_{leaf} < T_{air}$. However, as the denominator becomes large as g_{bH} and the degree of coupling increase, damping the degree of warming or cooling so T_{leaf} approaches T_{air}. Importantly, large *LE* (transpiration) is much more likely to occur when T_{air} and vapor pressure gradient (*VPD*) are high and g_{tot} is not depressed. However, transpiration depends critically on g_s, which is a fundamental leaf trait that varies widely by species and in response to environmental and physiological conditions, principally *VPD*, transpiration rate, and leaf water potential (23, 31–33). Critically, in almost all cases, g_s declines sharply with increasing *VPD*, often in a non-linear manner. Oren et al. (34) document a range of g_s-*VPD* relationships, from a tropical tree species like teak (*Tecton grandis*) with very high native g_s and *VPD* sensitivity to semi-arid acacia (*Acacia* spp.) trees with low native g_s and *VPD* sensitivity. Fauset et al. (35) also show large differences in this relationship for co-occurring montane tropical forest species that differ in other leaf traits critical for thermoregulation. Stomatal behavior also responds to other environmental factors, including light, CO_2 concentration, soil water deficit, and the hormone ABA (36).

For our purposes, we ignored CO_2 and ABA variations. We used a coupled photosynthesis-stomatal conductance model in the R package plantecophys (37) to simulate g_s values to use in the above T_{leaf} equations. We also tried the energy balance option in this package to simulate T_{leaf} but it systematically overestimated T_{leaf}, particularly at BCI. The coupled photosynthesis-stomatal conductance modeling used the optimality-based formulation with *VPD* dependence (33) to predict g_s as:

$$g_s = g_0 + 1.6(1 + \frac{g_1}{\sqrt{D}})\ \frac{A}{C_a} \qquad 11$$

where D is *VPD* (kPa), A is net leaf photosynthesis (μmol m^{-2} s^{-1}), C_a is the atmospheric CO_2 concentration (ppm), and g_0 and g_1 are fitted parameters (g_0 is typically set to 0). The slope, g_1, is proportional to the marginal water cost of carbon and the CO_2 compensation point and is thus inversely related to plant water use efficiency (33, 38).

We used this mechanistic photosynthesis-stomatal conductance model to explore T_{leaf}/T_{air} relationships using meteorological and radiation observations from two of our sites that contrast strongly in forest type and climate: a semi-arid pine forest in the Northwestern US (Metolius, OR), and a semi-deciduous tropical forest in Panama (BCI). The meteorological and radiation data used for T_{leaf} modeling were measured at the tower top and included the following variables: T_{air}, *VPD*, and downwelling *SW* and *LW* radiation. We used the Bigleaf R package to estimate *wind speed* at the top of the canopy using a logarithmic relationship, as this quantity is known to have large gradients between the canopy and the tower top. We chose 6-day periods at both sites when there was adequate soil volumetric water (> 0.2 m^3 m^{-3} at 30 cm, in the upper quartile at both sites). We used a g_1 value of 2.35 for the semi-arid pine site and 3.77 (the mean of tropical rainforest g_1 values) for BCI from (38). Values for the maximum RuBP carboxylation rate (V_{max}) measured at each site or nearby were similar (48 μmol m^{-2} s^{-1}) and based on (36) for Metolius and (39) for BCI.

At the semi-arid pine site, on an average basis, radiation fluxes and T_{air} are lower while *wind speed* and *VPD* are generally higher, as compared to the tropical forest site. Additionally, canopy structure and leaf characteristics are quite distinct at these sites: the pine site is characterized by a generally open forest canopy with low LAI and low tree species diversity, as well as small leaf sizes (with consequent higher atmospheric coupling) and low g_s; by contrast, the tropical forest site is characterized by a closed canopy with high tree species diversity and much larger leaf sizes (with consequently lower coupling) and high g_s. These site-specific physical and biological differences allow us to explore their influence on T_{leaf}, and specifically to better understand what controls the slope and the amount of hysteresis in the T_{leaf}/T_{air} relationship. While leaf size and g_s effects partially explain the differences in T_{can}/T_{air} hysteresis between the needle-leaf and broad-leaf forests, aspects of canopy structure are also important and not captured by our modeling. All photosynthesis-conductance and T_{leaf} modeling was conducted in R (version 4.0.0 -- "Arbor Day") using site-specific meteorological and radiation driving data.

Supplemental Figures and Tables

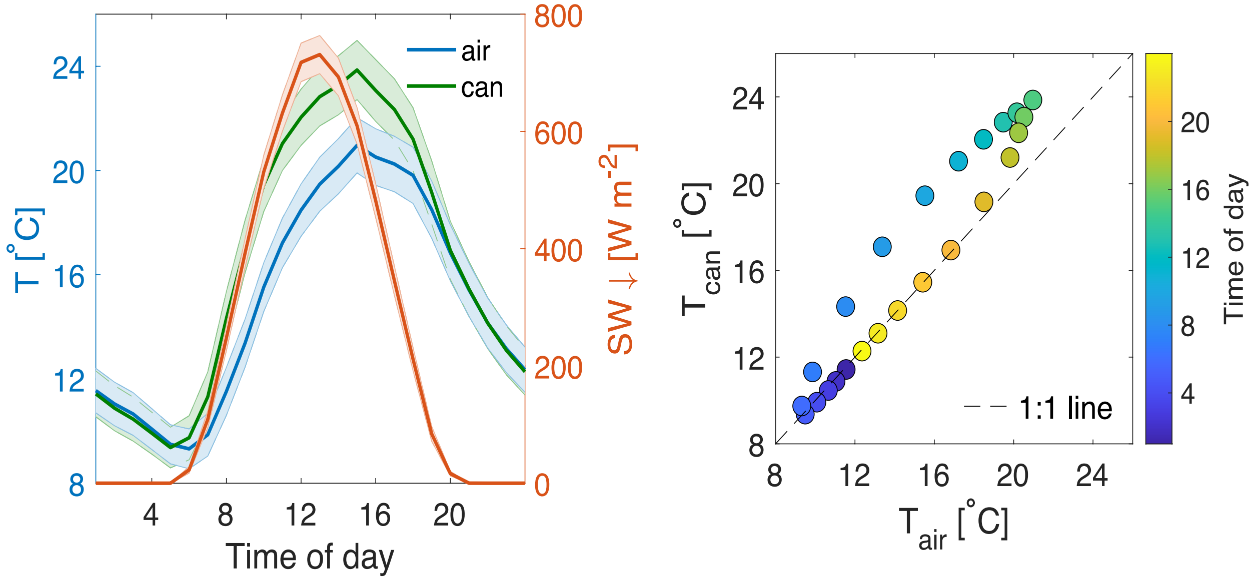

Figure S1. (a) Mean diel cycles of canopy T_{can}, T_{air} (both ºC), and shortwave irradiance (W m^{-2}) for the 2015 growing season (March 1-Sep 30) at Wind River with standard errors given by line shading. All times are PST. **(b)** Mean diel T_{can} plotted against mean diel T_{air} for the same period, color shaded by hour of day. The dashed line is the 1:1 line.

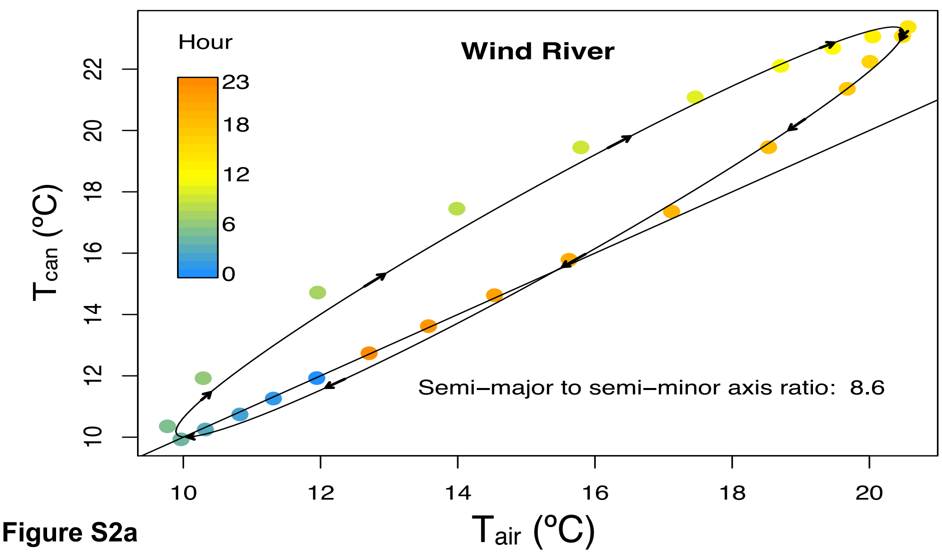

Figure S2a

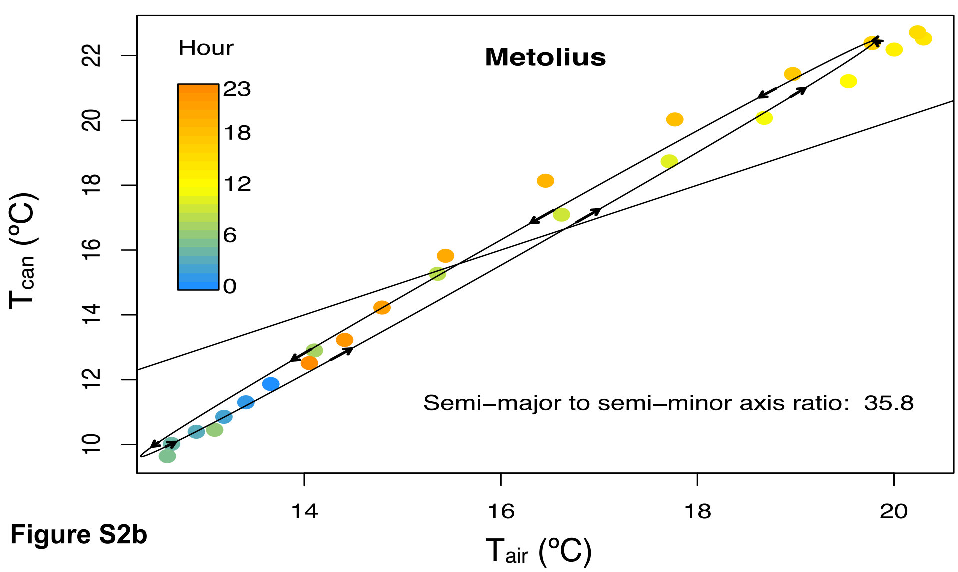

Figure S2b

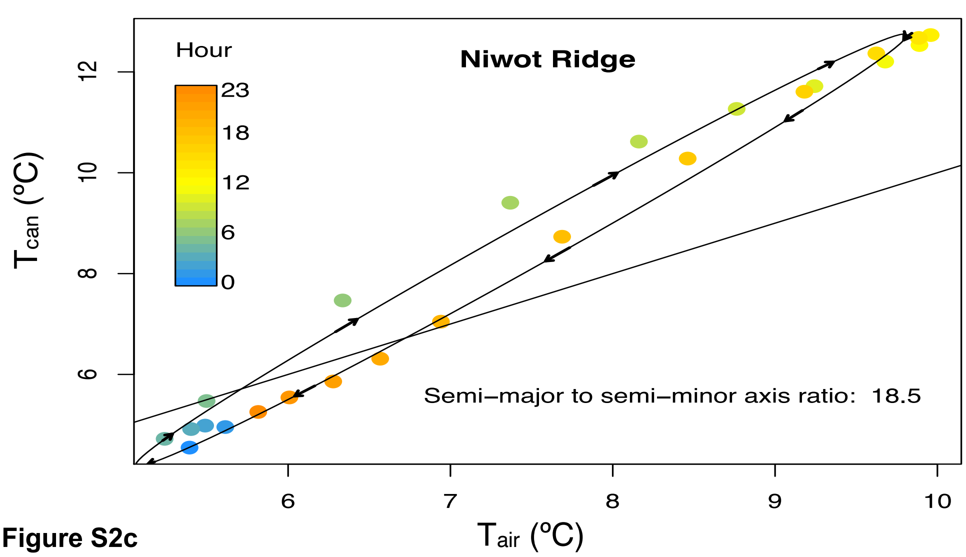

Figure S2c

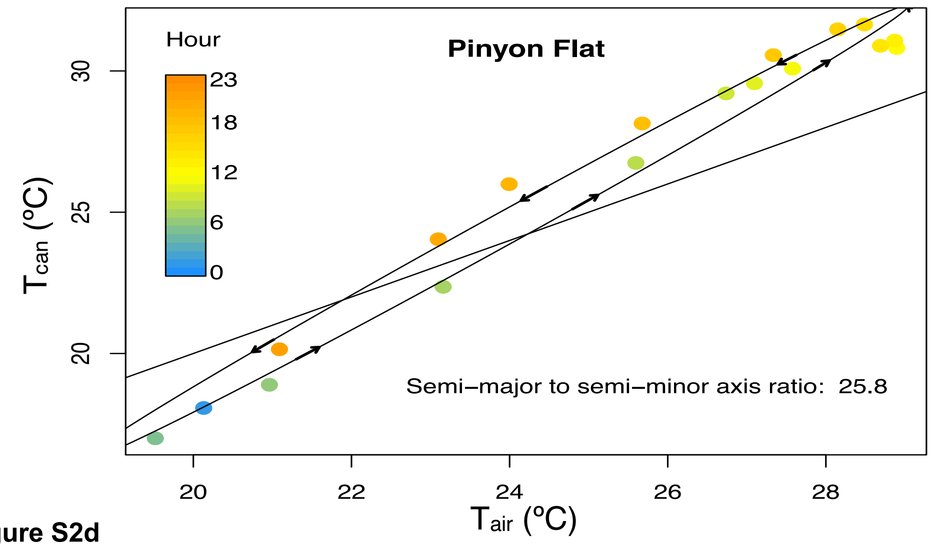

Figure S2d

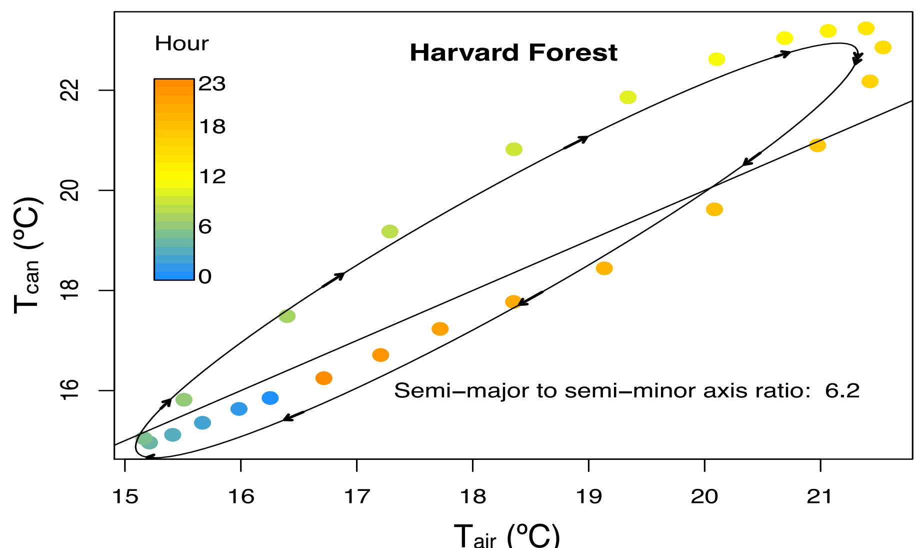

Figure S2e

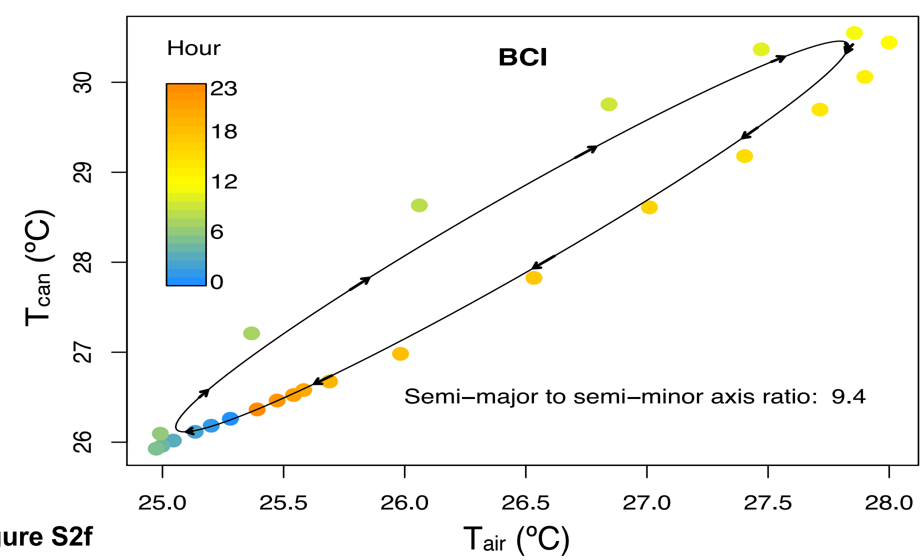

Figure S2f

Figure S2. Growing season mean diel T_{can} (ºC) plotted against mean diel T_{air} (ºC), color shaded by hour of day at Wind River **(a)**, Metolius **(b)**, Niwot Ridge **(c)**, Pinyon Flat **(d)**, Harvard Forest **(e)**, and BCI **(f)**. Semi-major to semi-minor axis ratios are calculated with T_{can} and T_{air} normalized by their maximum respective values so that sites with different seasonal temperature ranges can be compared. Hysteresis loops and axis ratios are generated with the R package "hysteresis" following (40). The solid line is the 1:1 line.

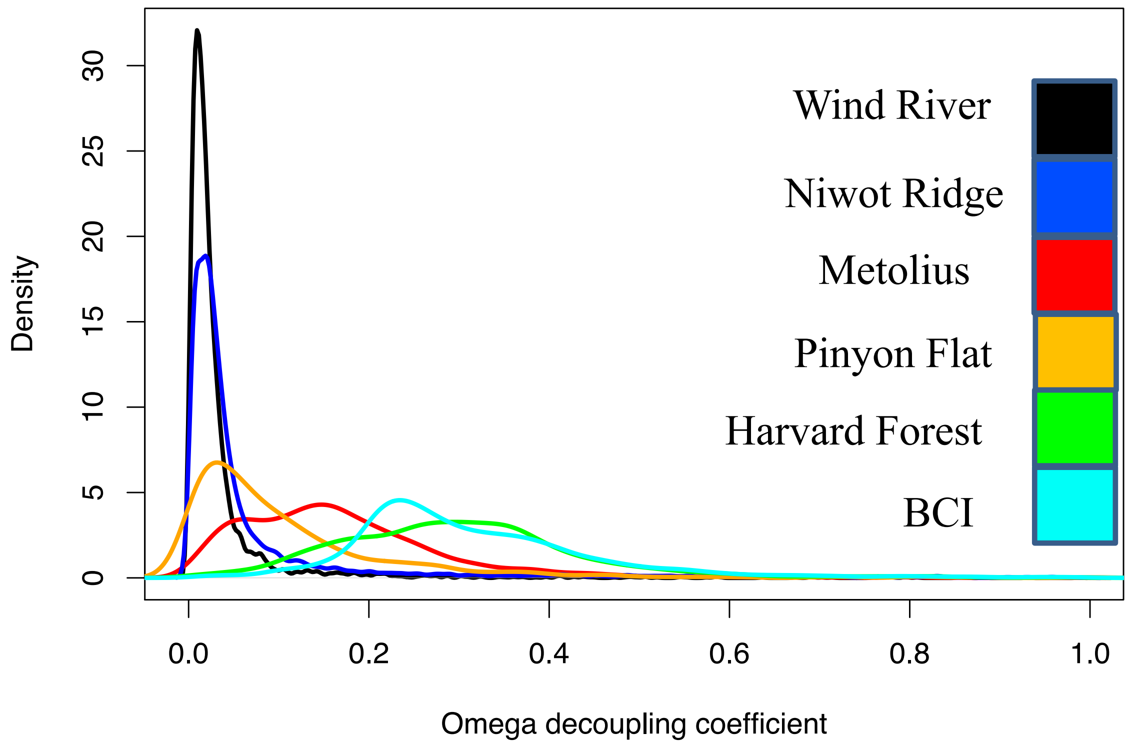

Figure S3. The canopy-scale omega decoupling coefficient for each site calculated with the R package, Bigleaf (16).

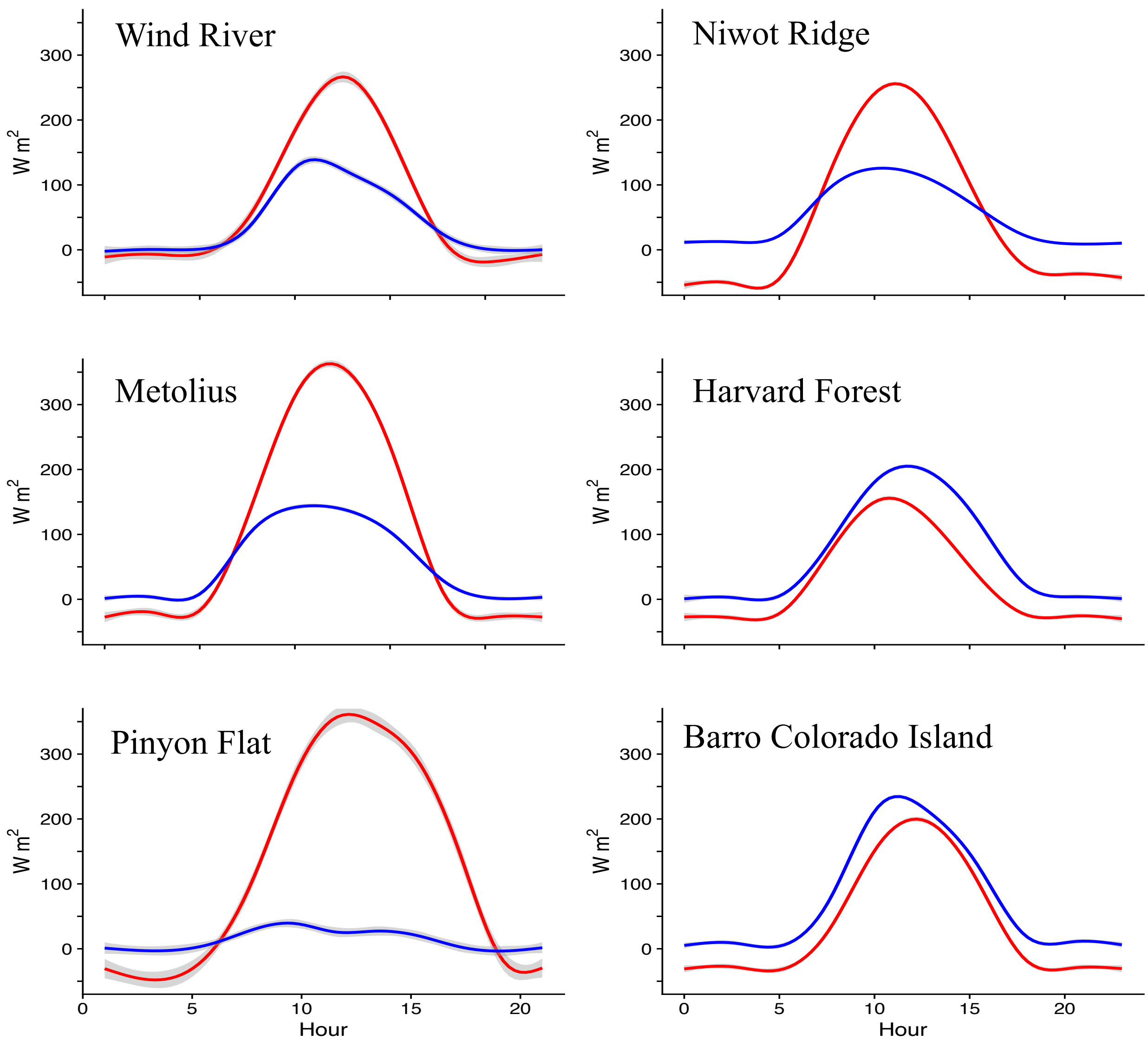

Figure S4. Mean growing season diurnal sensible (red line) and latent heat fluxes (both in $W\ m^{-2}$) for each site using the same time period of data for T_{can}. Shading around each line is the 95% CI using half-hourly flux data filtered consistent in the same way as the T_{can} analyses. A smoothed line fit using a generalized additive model (41) in R version 3.6.2 (R Core Team 2019).

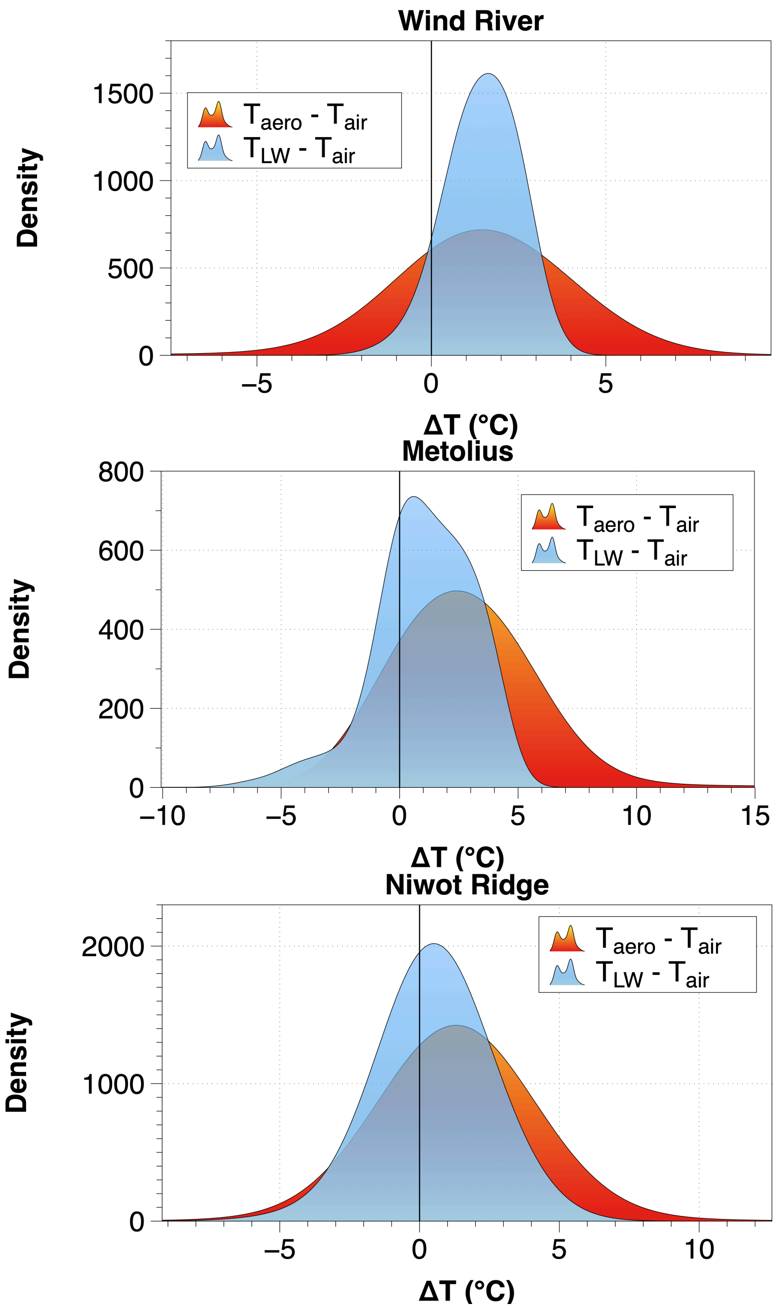

Wind River
Density
1500
1000
500
0
T_{aero} - T_{air}
T_{LW} - T_{air}
−5
0
5
ΔT (°C)
Metolius
Density
800
600
400
200
0
T_{aero} - T_{air}
T_{LW} - T_{air}
−10
−5
0
5
10
15
ΔT (°C)
Niwot Ridge
Density
2000
1000
0
T_{aero} - T_{air}
T_{LW} - T_{air}
−5
0
5
10
ΔT (°C)

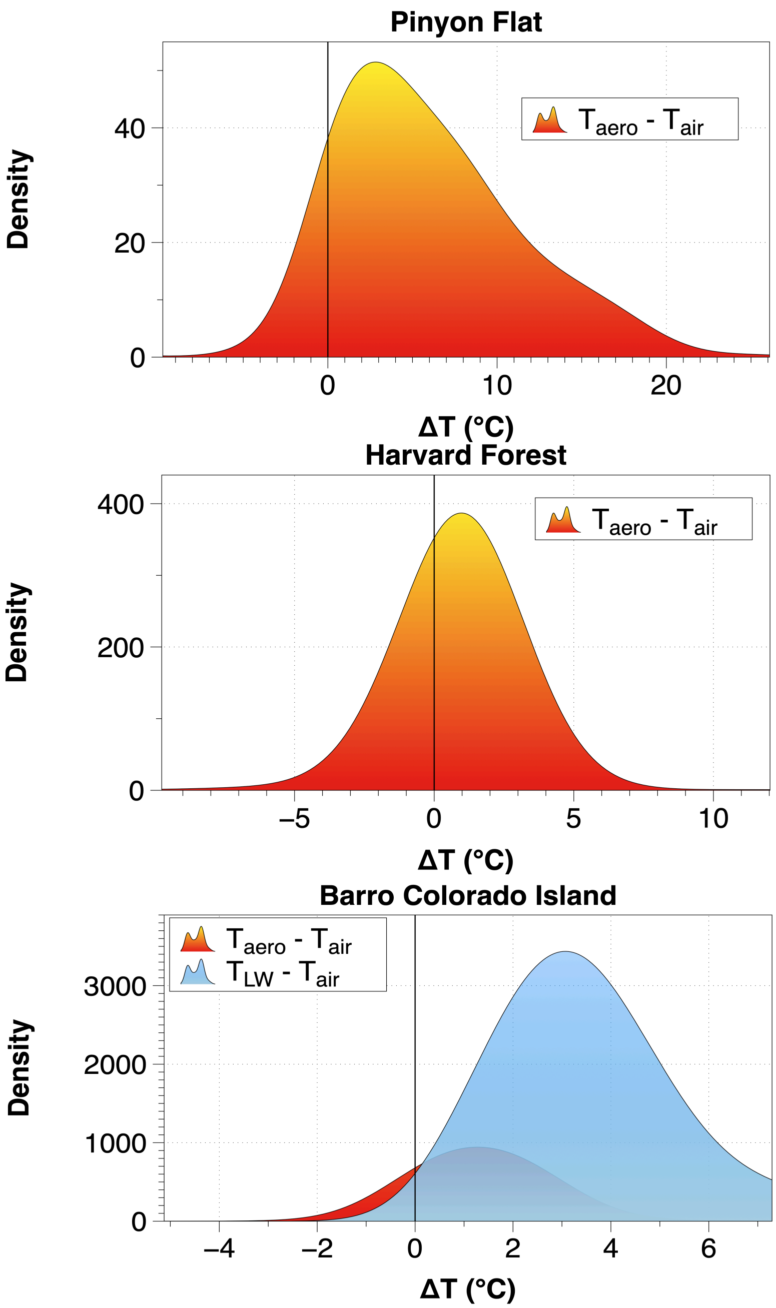

Figure S5. Probability density histograms of various daytime canopy and surface temperature metrics minus T_{air} at all of our sites. The smoothed orange histograms refer to (T_{aero} - T_{air}) at all sites, where T_{aero} is the aerodynamic temperature calculated from eddy covariance measurements of sensible heat flux, windspeed, and friction velocity. The smoothed light blue histograms represent (T_{LW} - T_{air}) at Wind River, Metolius, and Niwot Ridge, where T_{LW} is the surface radiometric temperature calculated from available measurements of upwelling longwave radiation measured by radiometers on the towers. Only daytime flux, meteorological, and radiation data when downwelling shortwave radiation exceeded 25 W m^{-2} were included in these analyses.

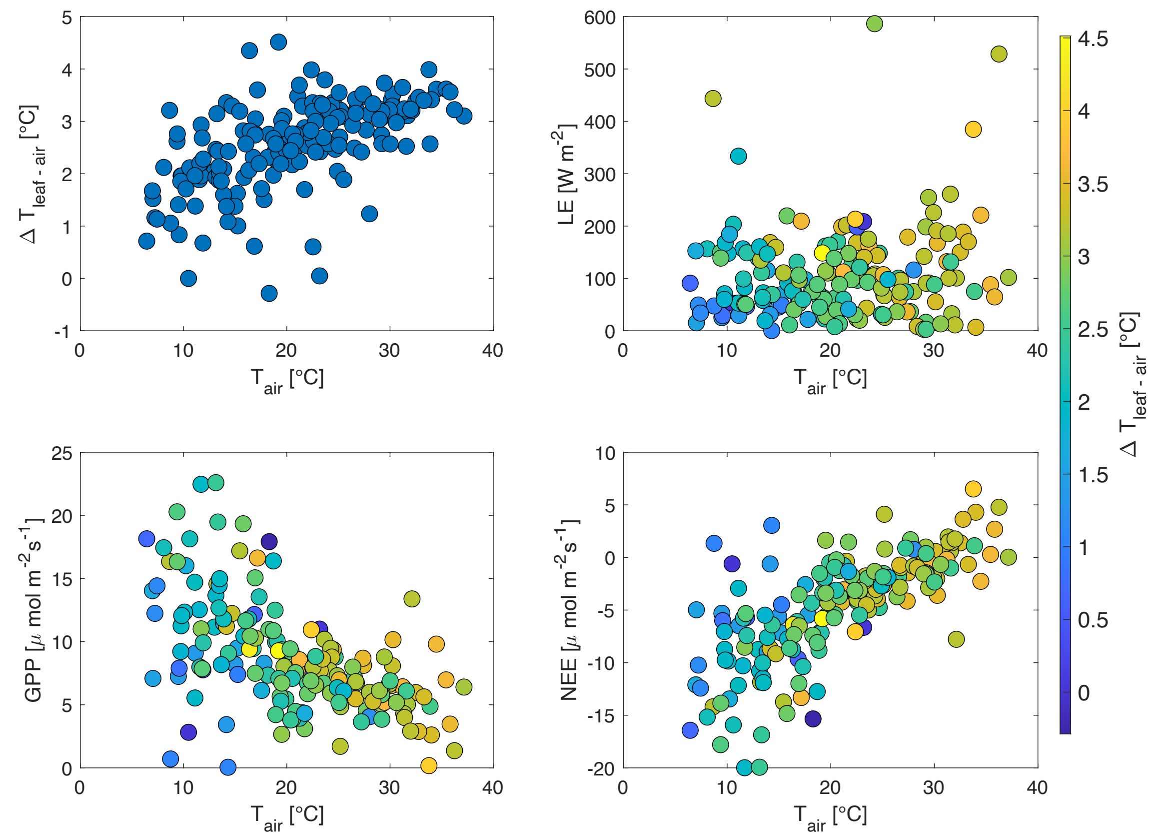

Figure S6. Relationships between daily maximum T_{air} and (T_{can} - T_{air}), latent heat (W m^{-2}), and NEE and GPP (μmol m^{-2} s^{-1}) during the 2015 growing season (Mar-Sep) at Wind River.

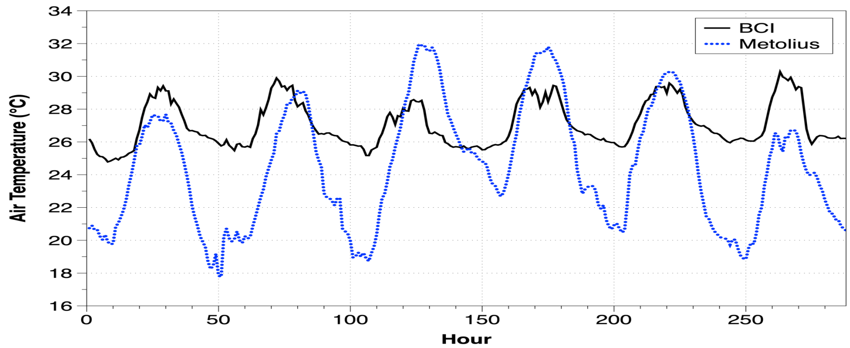

Figure S7a

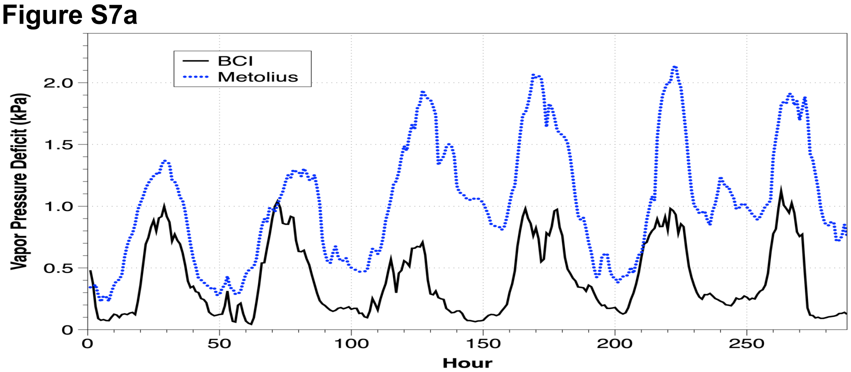

Figure S7b

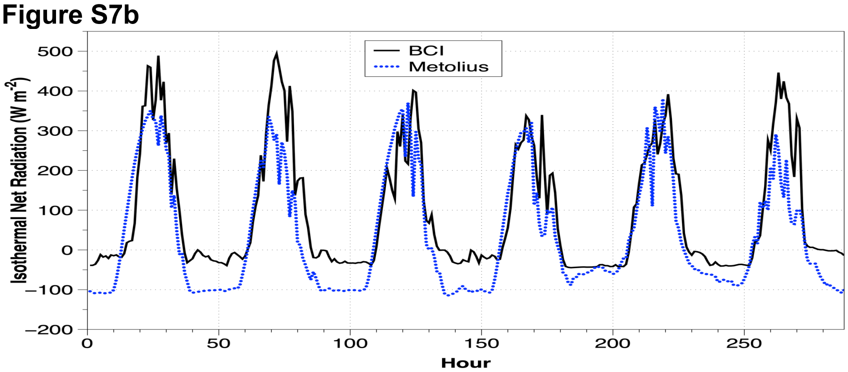

Figure S7c

Figure S7. Observed meteorological and radiation data used to drive leaf temperature models at Metolius (dashed blue line) and BCI (solid black line). **(a)** air temperature (ºC), **(b)** atmospheric vapor pressure deficit (kPa), and **(c)** isothermal net radiation (W m^{-2}).

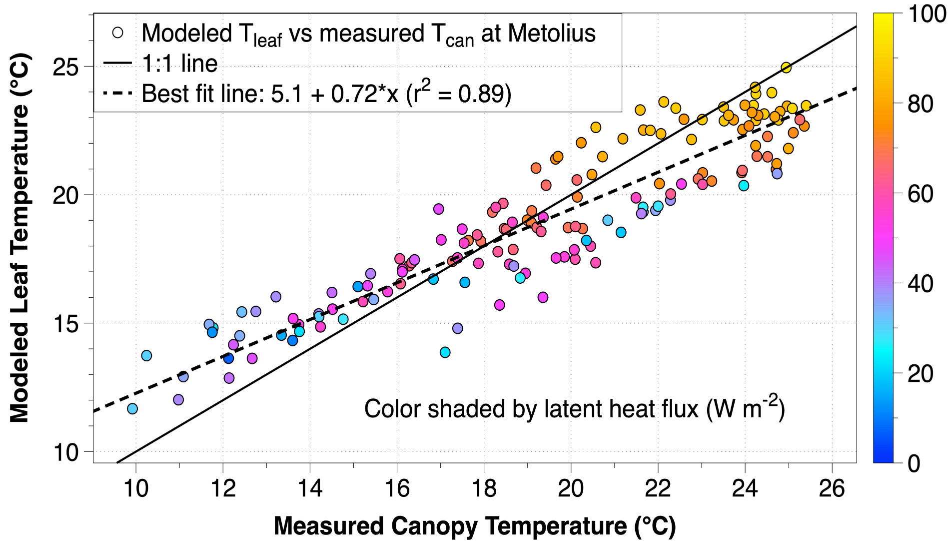

Figure S8a

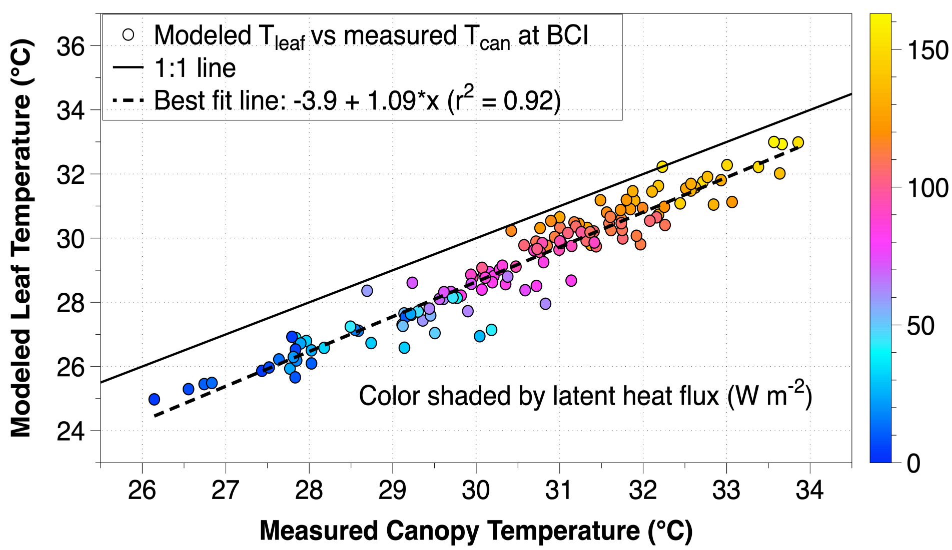

Figure S8b

Figure S8. Modeled T_{leaf} versus measured T_{can} (ºC) at Metolius **(a)** during a rain-free period (May 25-June 1, 2015) and BCI **(b)** for a period in the wet season (June 12-18, 2015). Color shading in both figures is by transpiration (W m^{-2}) during daytime conditions (downwelling shortwave radiation threshold of 25 W m^{-2}).

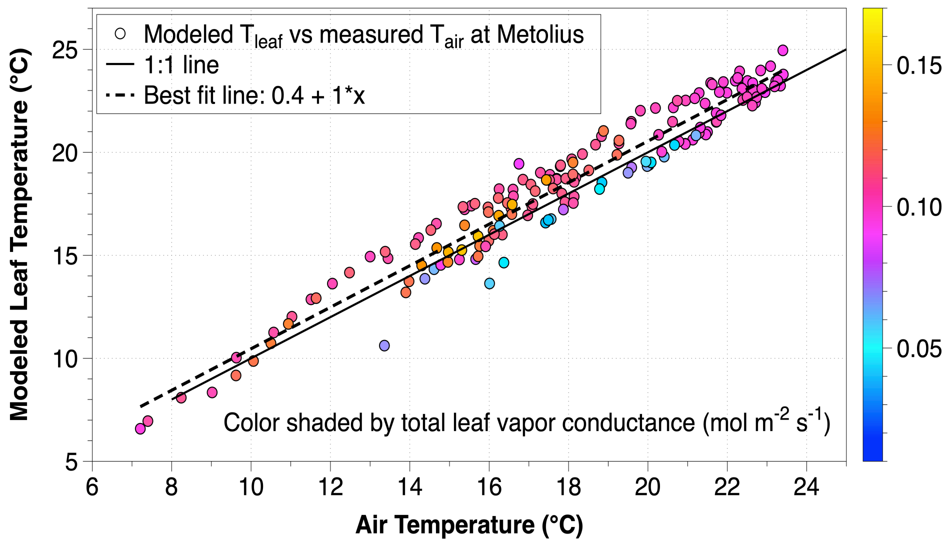

Figure S9a

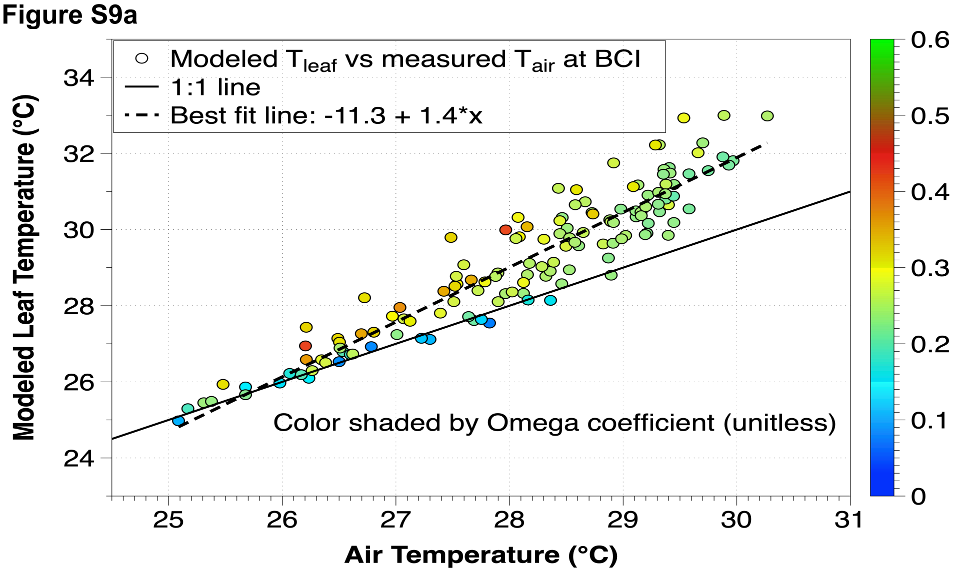

Figure S9b

Figure S9. Modeled T_{leaf} versus measured T_{air} (ºC) at Metolius **(a)** during a rain-free period (May 25-June 1, 2015) with shading by total water vapor leaf conductance (mol m^{-2} s^{-1}) and at BCI (**b)** for a period in the wet season (June 12-18, 2015) with color shading by the omega decoupling factor (unitless).

Table S1. Summary of forest climate and biotic characteristics. MAT and MAP indicate mean annual temperature and mean annual precipitation, respectively. LAI is leaf area index (m^2 m^{-2}).

Site	Forest ecosystem type	Climate classification	Location	Elevation (m)	MAT (°C)	MAP (mm)	LAI	Mean tree height (m)
Metolius	semi-arid temperate second-growth conifer forest	Mediterranean	44.4523 N -121.5574 E	1253	6.3	523	2.8	18
Wind River	moist temperate old-growth conifer forest	Mediterranean	45.8205 N -121.9519 E	371	8.8	2200	9.2	50-60
Niwot Ridge	subalpine evergreen needleleaf forest	Subarctic	40.0329 N -105.5464 E	3050	1.5	800	3.8 - 4.2	12-13
Pinyon Flat	arid conifer woodland	Warm Mediterranean	33.6047 N -116.4527 E	1281	15.8	316	-	
Harvard Forest	moist temperate forest with deciduous broadleaf and evergreen needleleaf trees	Warm Summer Continental	42.5378 N -72.1715 E	340	6.6	1150	3-4	18
Barro Colorado Island	tropical forest with deciduous and evergreen broadleaf trees	Tropical Rain Forest	9.154 N -79.848 E	150	26.0	2640	6.0	25

Table S2. Forest site descriptions

Site name	Forest characteristics
Metolius	The Metolius site (hereafter, MR) is located in a mature coniferous forest in central Oregon at an elevation of 1253 m asl. The study forest is designated as a core research site in the AMERIFLUX network (site US-Me2) where microclimate and eddy covariance flux measurements are collected from a flux tower. The canopy is dominated by ponderosa pine trees (*Pinus ponderosa*) with a few scattered incense cedar trees (*Calocedrus decurrens*). Trees are evenly distributed and the mean tree density is approximately 339 trees ha^{-1} (42). The climate is semi-arid, with warm and dry summers and cool and wet winters, with most precipitation occurring as snow or rain during the winter and spring (November through April). Additional descriptions of the study site, as well as information on site instrumentation and measurements, can be found in (7, 43)
Wind River	The Wind River site (hereafter, WR) is an Experimental Forest located in southwest Washington state, USA at an elevation of 371 m asl. This site has been registered as an AMERIFLUX network site (US-Wrc) since 1998 and is a NEON Core Site. The forest is 478 ha of preserved old-growth (~500 years old) evergreen needle-leaf forest, with two dominant tree species: Douglas fir (*Pseudotsuga menzesii*) and western hemlock (*Tsuga hetrophylla*). The forest has a stand density of 427 trees ha^{-1} and basal area of 82.9 m^2 ha^{-1}. Douglas-fir dominates the forest in basal area (~43%) and wood volume (~50%). This results in a bimodal distribution of LAI (44), with peaks centered at 35m and 15m respectively. Details of sensor measurements are reported elsewhere (9).
Niwot Ridge	The Niwot Ridge Subalpine Forest site (hereafter, NW) is an AmeriFlux site (US-NR1, 1998-present) located in the Rocky Mountains of Colorado (40° 1' 58.349'' N,105° 32' 49.095'' W, Elevation: ~3050m). The tower (height 26m) is surround by mix of evergreen needleleaf species: lodgepole pine (*Pinus contorta* Douglas ex Loudon), Engelmann spruce (*Picea engelmannii* Parry ex Engelm.), and subalpine fir (*Abies lasiocarpa* (Hook.) Nutt.). Smaller patches of aspen (*Populus tremuloides*) and limber pine (*Pinus flexilis*) are also present. The tree density near the tower is ~4000 trees ha^{-1} (Monson et al. 2010). Though the terrain within 5 km of the site can be quite steep, the tower is located in a relatively flat area with an approximate topographic slope angle of 4.3°. From November-February, the weather at the site is characterized by cold mid-continental conditions and strong downslope winds are frequent. Snow usually covers the ground from early November until late May. Further details about the US-NR1 site are documented elsewhere (11, 12).
Pinyon Flat Juniper	Arid conifer woodland composed of a mix of juniper (*Juniperus sp.*) and pinyon pine (*Pinus monophylla*) trees and associated shrubs and grasses.
Harvard Forest	The Harvard Forest site (HF) is a mixed temperate forest located in rural central Massachusetts, USA, about 100 km west of the city of Boston. Mixed forest stands surrounding the tower are dominated by the deciduous species red oak (*Quercus rubra* L., ∼40% of basal area) and red maple (*Acer rubrum* L., ∼20% of basal area). Evergreen white pine (*Pinus strobus* L.) is the dominant conifer.
Barro Colorado Island	The Barro Colorado Island site (BCI) forest site in Panama (9°9′ N, 79°50′ W). The forest is semi-deciduous with has high biodiversity (~300 species of trees and 162 species of lianas in 50 ha). The climate is characterized by a dry season from mid-December to mid-April, during which about 20% of canopy trees are leafless resulting in a moderate seasonal variation of LAI. Above-ground biomass 140 Mg C ha^{-1} (45).

SI References

1. D. M. Aubrecht, *et al.*, Continuous, long-term, high-frequency thermal imaging of vegetation: Uncertainties and recommended best practices. *Agric. For. Meteorol.* **228–229** (2016).
2. M. G. J. Tattersall, L. True, Package ‘ Thermimage ’ (2016).

3. Y. Kim, *et al.*, Canopy skin temperature variations in relation to climate, soil temperature, and carbon flux at a ponderosa pine forest in central Oregon. *Agric. For. Meteorol.* **226–227** (2016).
4. D. R. Bowling, *et al.*, Limitations to winter and spring photosynthesis of a Rocky Mountain subalpine forest. *Agric. For. Meteorol.* **252**, 241–255 (2018).
5. S. Pau, M. Detto, Y. Kim, C. J. Still, Tropical forest temperature thresholds for gross primary productivity. *Ecosphere* **9**, 1–12 (2018).
6. C. J. Still, *et al.*, Imaging canopy temperature: shedding (thermal) light on ecosystem processes. *New Phytol.* (2021) https:/doi.org/10.1111/nph.17321.
7. H. Kwon, B. E. Law, C. K. Thomas, B. G. Johnson, The influence of hydrological variability on inherent water use efficiency in forests of contrasting composition, age, and precipitation regimes in the Pacific Northwest. *Agric. For. Meteorol.* **249**, 488–500 (2018).
8. C. K. Thomas, *et al.*, Seasonal hydrology explains interannual and seasonal variation in carbon and water exchange in a semiarid mature ponderosa pine forest in central Oregon. *J. Geophys. Res. Biogeosciences* **114**, 1–22 (2009).
9. S. Wharton, M. Falk, K. Bible, M. Schroeder, K. T. Paw U, Old-growth CO 2 flux measurements reveal high sensitivity to climate anomalies across seasonal, annual and decadal time scales. *Agric. For. Meteorol.* **161**, 1–14 (2012).
10. S. P. Burns, T. W. Horst, L. Jacobsen, P. D. Blanken, R. K. Monson, Using sonic anemometer temperature to measure sensible heat flux in strong winds. *Atmos. Meas. Tech.* **5**, 2095–2111 (2012).
11. R. K. Monson, *et al.*, Carbon sequestration in a high-elevation, subalpine forest. *Glob. Chang. Biol.* **8**, 459–478 (2002).
12. S. P. Burns, P. D. Blanken, A. A. Turnipseed, J. Hu, R. K. Monson, The influence of warm-season precipitation on the diel cycle of the surface energy balance and carbon dioxide at a Colorado subalpine forest site. *Biogeosciences* **12**, 7349–7377 (2015).
13. S. Urbanski, *et al.*, Factors controlling CO2 exchange on timescales from hourly to decadal at Harvard Forest. *J. Geophys. Res. Biogeosciences* **112**, 1–25 (2007).
14. M. Detto, D. Baldocchi, G. G. Katul, Scaling Properties of Biologically Active Scalar Concentration Fluctuations in the Atmospheric Surface Layer over a Managed Peatland. *Boundary-Layer Meteorol.* **136**, 407–430 (2010).
15. G. Lasslop, *et al.*, Separation of net ecosystem exchange into assimilation and respiration using a light response curve approach: Critical issues and global evaluation. *Glob. Chang. Biol.* **16**, 187–208 (2010).
16. J. Knauer, T. S. El-Madany, S. Zaehle, M. Migliavacca, Bigleaf—An R package for the calculation of physical and physiological ecosystem properties from eddy covariance data. *PLoS One* **13**, 1–26 (2018).
17. A. M. Young, *et al.*, Seasonality in aerodynamic resistance across a range of North American ecosystems. *Agric. For. Meteorol.* **310**, 108613 (2021).
18. D. M. Gates, Energy Exchange and Ecology. *Bioscience* **18**, 90–95 (1968).
19. G. S. Campbell, J. M. Norman, *An Introduction to Environmental Biophysics*, Second (Springer-Verlag, 1998).
20. J. Monteith, M. Unsworth, *Principles of environmental physics: plants, animals, and the atmosphere.* (Academic Press, 2013).
21. H. G. Jones, *Plants and microclimate: a quantitative approach to environmental plant physiology* (Cambridge University Press, 2014).
22. P. G. Jarvis, K. G. Mcnaughton, Stomatal Control of Transpiration: Scaling Up from Leaf to Region. *Adv. Ecol. Res.* **15**, 1–49 (1986).
23. R. LEUNING, F. M. KELLIHER, D. G. G. DE PURY, E. -D SCHULZE, Leaf nitrogen, photosynthesis, conductance and transpiration: scaling from leaves to canopies. *Plant. Cell Environ.* **18**, 1183–1200 (1995).
24. N. Dong, I. C. Prentice, S. P. Harrison, Q. H. Song, Y. P. Zhang, Biophysical homoeostasis of leaf temperature: A neglected process for vegetation and land-surface modelling. *Glob. Ecol. Biogeogr.* **26**, 998–1007 (2017).
25. R. Pieruschka, G. Huber, J. A. Berry, Control of transpiration by radiation. *Proc. Natl. Acad. Sci. U. S. A.* **107**, 13372–13377 (2010).

26. P. Martin, The significance of radiative coupling between vegetation and the atmosphere. *Agric. For. Meteorol.* **49**, 45–53 (1989).
27. S. T. Michaletz, *et al.*, The energetic and carbon economic origins of leaf thermoregulation. *Nat. Plants* **2** (2016).
28. G. B. Bonan, *Ecological climatology: Concepts and applications*, Second Edi (Cambridge University Press, 2016).
29. F. M. Kelliher, R. Leuning, M. R. Raupach, E. D. Schulze, Maximum conductances for evaporation from global vegetation types. *Agric. For. Meteorol.* **73**, 1–16 (1995).
30. I. J. Wright, *et al.*, Global climatic drivers of leaf size. *Science (80-.).* **357**, 917–921 (2017).
31. F. C. Meinzer, *et al.*, Atmospheric and hydraulic limitations on transpiration in Brazilian cerrado woody species. *Funct. Ecol.* **13**, 273–282 (1999).
32. T. N. Buckley, The control of stomata by water balance. *New Phytol.* **168**, 275–292 (2005).
33. B. E. Medlyn, *et al.*, Reconciling the optimal and empirical approaches to modelling stomatal conductance. *Glob. Chang. Biol.* **17**, 2134–2144 (2011).
34. R. Oren, *et al.*, Survey and synthesis of intra- and interspecific variation in stomatal sensitivity to vapour pressure deficit. *Plant, Cell Environ.* **22**, 1515–1526 (1999).
35. S. Fauset, *et al.*, Differences in leaf thermoregulation and water use strategies between three co-occurring Atlantic forest tree species. *Plant Cell Environ.* **41**, 1618–1631 (2018).
36. P. J. Franks, J. A. Berry, D. L. Lombardozzi, G. B. Bonan, Stomatal function across temporal and spatial scales: Deep-time trends, land-atmosphere coupling and global models. *Plant Physiol.* **174**, 583–602 (2017).
37. R. A. Duursma, Plantecophys - An R package for analysing and modelling leaf gas exchange data. *PLoS One* **10**, 1–13 (2015).
38. Y. S. Lin, *et al.*, Optimal stomatal behaviour around the world. *Nat. Clim. Chang.* **5**, 459–464 (2015).
39. J. Wu, *et al.*, The response of stomatal conductance to seasonal drought in tropical forests. *Glob. Chang. Biol.* **26**, 823–839 (2020).
40. F. Yang, A. M. Parkhurst, Efficient Estimation of Elliptical Hysteresis with Application to the Characterization of Heat Stress. *J. Agric. Biol. Environ. Stat.* **20**, 371–388 (2015).
41. H. Wickham, ggplot2.
42. J. Irvine, B. E. Law, J. G. Martin, D. Vickers, Interannual variation in soil CO2 efflux and the response of root respiration to climate and canopy gas exchange in mature ponderosa pine. *Glob. Chang. Biol.* **14**, 2848–2859 (2008).
43. B. E. Law, *et al.*, Carbon dioxide and water vapor exchange by young and old ponderosa pine ecosystems during a dry summer. *Tree Physiol.* **21**, 299–308 (2001).
44. G. G. Parker, *et al.*, Three-dimensional structure of an old-growth Pseudotsuga-tsuga canopy and its implications for radiation balance, microclimate, and gas exchange. *Ecosystems* **7**, 440–453 (2004).
45. M. Detto, S. J. Wright, O. Calderón, H. C. Muller-Landau, Resource acquisition and reproductive strategies of tropical forest in response to the El Niño-Southern Oscillation. *Nat. Commun.* **9**, 1–8 (2018).